Article

Research on the Mechanism and Characteristics of Ultrasonically Coupled Mechanical Rock-Breaking Pre-Fracturing Technology

Chengwen Liu [1,†], Mingyu Duan [1,†] , Yizhe Huang [1,2], Qibai Huang [1], Jiaqi Liu [1], Zhicheng Wang [1] and Zhifu Zhang [3,*]

1   School of Mechanical Science and Engineering, Huazhong University of Science and Technology, Wuhan 430074, China; m202270419@hust.edu.cn (C.L.); duanmingyu@hust.edu.cn (M.D.); yizhehuang@hbut.edu.cn (Y.H.); qbhuang@hust.edu.cn (Q.H.); m202270418@hust.edu.cn (J.L.); m202270816@hust.edu.cn (Z.W.)
2   School of Mechanical Engineering, Hubei University of Technology, Wuhan 430068, China
3   School of Mechanical and Electrical Engineering, Hainan University, Haikou 570228, China
*   Correspondence: 996099@hainanu.edu.cn
†   These authors contributed equally to this work.

Abstract: In this paper, we propose an ultrasonically coupled mechanical rock-breaking technology, creatively design an ultrasonically coupled mechanical rock-breaking drum, concurrently develop an ultrasonic cracking simulation method based on test coordination, and study the cracking mechanism and characteristics of ultrasonically pre-broken rock in order to increase the rock-breaking efficiency of shearer drums and lengthen pickaxe service life. To further understand the theory behind ultrasonic-coupled mechanical rock breaking, the operation of a fusion drum and the implications of ultrasonic field theory in a solid medium are first examined. Second, the impact and mechanism of the ultrasonic pre-crushing of the target red sandstone are investigated in conjunction with conducting a rock uniaxial compression test and RFPA^{2D} modeling. Furthermore, an ultrasonic pre-crushing fracturing mechanism test of the target red sandstone further reveals the effect and mechanism of ultrasonic fracturing. The efficacy of ultrasonic-coupled mechanical single-cutter cutting is then investigated using the discrete element cutting model (PFC^{2D}) of red sandstone. The results show that under the action of ultrasonic waves with an excitation frequency of 41 kHz, cracks can effectively be produced inside the rock mass of the target red sandstone, and the cumulative amount of acoustic emission is as high as 513, which reduces the strength of the rock mass and disintegrates its internal structure; the average cut-off force of the purely mechanical rock-breaking mode is 6374 N, and that of ultrasonically coupled rock breaking is 4185 N, which is a reduction of 34.34%, and can be attributed to the fact that ultrasonic waves can loosen the structure of the rock mass. This is explained by the ability of ultrasonic vibrations to weaken the structure of rock. The coupled rock-breaking technology not only simplifies mechanical cutting and rock breaking but the lower force can also reduce a pick-shaped trunnion's wear failure cycle. This improves the environment for subsequent pick-shaped trunnion cutting and rock breaking and prevents the pick-shaped trunnion from being subjected to high-stress loads for an extended period of time so as to prolong its working life.

Keywords: ultrasonic pre-crushing; shearer drum; conical picks; coupled rock breaking

1. Introduction

Different types of rock with varying degrees of hardness are involved in the coal rock-mining process. In particular, when mining deep coal seams, high-hardness rock like gangue rock has a significant impact on how effectively high-quality coal is mined. China's coal resources are abundant, but with the increase in mining depth, coal seams change in terms of the existence of increasing difficulties, for example, mining difficulty

gradually increases; coal seam gangue is more abundant; faults increase; part of the gangue solidity coefficient increases to 12 or more [1], especially when encountering more-intact rock; and the use of traditional coal-mining machine pick-axe-shaped cut-off teeth impact rock breaking is rendered inefficient, resulting in serious losses; thus, relying on pick-axe-shaped cut-off teeth impact rock-breaking continuous mining is extremely difficult, and the economy of its applicability is poor [2]. As a result, the mining industry now faces a significant challenge related to how to effectively and swiftly crush rocks, which has also turned into a focus of research for scientists from many nations.

1.1. Overview of Purely Mechanical Rock-Breaking Methods

There are two main categories of solely mechanical rock-breaking techniques: mechanical rock-breaking techniques and conventional drilling and blasting methods. Regarding the traditional drilling and blasting methods, Xu et al. [3] showed that the differential time, the depth of the package, the form of the charge employed, and the relevant blasting parameters have a large effect on blasting vibrations. At present, research on blasting vibration mostly remains in the experimental stage and lacks theoretical or numerical-simulation-based support. For example, in differential blasting, there is a lack of research on the change law of blasting vibration under different detonation sequence conditions, and there is no research on the change law of blasting vibration for different charge forms. Drilling and blasting design mainly rely on experience. Drilling and blasting methods cannot be continuously employed, and blasting construction lacks mechanization, automation, and refinement; has a low degree of digitization; and poses safety hazards.

Impact rock breaking, cutting rock breaking, and rolling rock breaking are the three subtypes of mechanical rock breaking. According to the form of crushing, impact rock breaking can be classified as chiseling, smashing, splitting, or shooting. Based on these advantages, people have created numerous impact tools (such as picks, hammers, and chisels) that are effective and time and labor saving. Cutting rock breaking is a method of rock breaking in which a tool is applied directly to the rock, using the blade to cut and separate material from the outer surface of the rock. Rolling rock breaking is a composite mechanical rock-breaking method in which the tool crushes the rock under great pressure and inflicts shear crushing of the rock via the movement of the tool. Li et al. [4] revealed that mechanical rock breaking can effectively solve many problems encountered in blasting rock breaking, but its equipment and tools are expensive, and the tools must be able to deal with the poor wear resistance of hard rock, resulting in high maintenance costs and huge investments, thus limiting the applications of mechanical rock-breaking methods. Ferri Hassani et al. [5] point out that when crushing hard rock with high strength, not only are mechanical rock-breaking methods inefficient and ineffective in terms of breaking rock, but the wear and tear of the tool is suddenly a prominent problem, and the higher maintenance cost and workload, as well as the lower rock intrusion rate, are the main problems that are difficult to overcome using mechanical rock-breaking methods.

Even though mechanical rock-breaking methods have been developed for decades and their corresponding efficiency and reliability have been continuously improved, constituting great progress compared to the initial stage, the inherent issues of low rock-breaking efficiency, slow drilling speed, and the high wear and tear of the corresponding machine tools have gradually led to bottlenecks, and it is difficult to make significant breakthroughs, leading to a failure to meet the needs of today's mining operations. Therefore, the focus of academic study has steadily switched to new techniques for efficiently breaking rocks or to the development of auxiliary tools.

1.2. Overview of New Rock-Breaking Technologies

In terms of novel design, new methodologies, and advanced technologies, geotechnical engineering technology in the field of mining engineering has advanced significantly in recent years. The new rock-breaking technology can mainly be divided into two categories: one category is the use of primarily thermal energy to break rock, like laser and microwave

rock breaking, while the other category is still predominantly based on using mechanical energy to break rock, such as hydraulic and ultrasonic rock breaking.

Laser rock breaking is a technique for breaking rock via exposing the rock surface to a high-energy laser beam. For example, the studies by Guo et al. [6] and Zheng et al. [7] show that laser rock breaking is more effective in breaking rock than conventional mechanical rock-breaking techniques when faced with hard rock. However, this technology has not yet reached a point of widespread commercialization or industrialization because of the high cost of high-energy lasers, the difficulty of long-distance laser transmission in downhole environments, and the narrow field of the corresponding laser's action.

The microwave rock-breaking technique is a method that involves using microwaves to heat rocks and thus induce rock damage. Gwarek W.K. et al.'s [8] study showed that the wavelength of electromagnetic wave heating commonly used in microwave rock breaking is 0.915 m, while the commonly used frequency is 2.45 GHz. Gao et al. [9] found that granite under a microwave field exhibits high-temperature melting and fracture, and the highest temperature can reach 550 °C under the irradiation of circulating microwaves. A minimum irradiation time threshold of 3 min is needed to cause irreversible damage to this rock. Osepchuk J.M. [10] reported that the microwave-heating principle consists of an object's internal polar molecules in an electromagnetic field under the action of a high-frequency reciprocating motion, generating heat, so microwave heating has the advantages of fast warming, without contact and medium transfer, and a strong penetration capacity, but Jones D.A. et al. [11] point out that the microwave-heating power in daily use is small, and at this range of power, it is difficult to crush rock in a manner that meets engineering needs in a short period of time. Clark D.E. et al. [12] concluded that with regard to simply increasing the power needed to use an ultra-high-power magnetron in microwave breaking, in addition to lowering the purchase cost and other rising costs, there is a lack of stability of the shortcomings.

Hydrodynamic rock breaking is a method in which high-pressure water jets are used to impact rock in order to break it. Han [13] studied the effect of using water jets at different speeds, angles of incidence, and diameters on the efficiency of impact rock breaking and concluded that the best rock-breaking effect was achieved when the angle of incidence of the jet was around 75°. Li et al. [14], through a large number of experimental studies, showed that the advantages of water jets in assisting mechanical cutting rock crushing stemmed from a water jet's cutting groove, which can increase the free surface of rock, thus reducing the mechanical cutting force, increasing the depth of a cut, improving the speed of rock breaking, and allowing the employed tool to cool, reducing the cutting temperature and the possibility of tool wear and brittle damage, thereby prolonging the service life of a tool by preventing friction and fire and controlling dust and reducing noise. However, Fan et al. [15] found that it was difficult to break hard rock over a large area because high-pressure water jets are powered by high-pressure water pumps, which are limited in terms of pumping pressure. The aforementioned innovative rock-breaking techniques can fracture practically all types of rocks found in nature, and they also avoid mechanical rock-breaking issues like disturbance. However, because of their high cost and insufficient technological advancement, these rock-breaking techniques cannot yet be widely adopted.

1.3. Overview of Ultrasonic High-Frequency-Vibration Rock-Breaking Methods

It is important to note that rock has an intrinsic frequency between 7 and 20 kHz, which is right in the range of ultrasonic waves, making it possible to crush rock using ultrasonic waves [16]. Rock can be vibrated and stimulated to enable fracture simulation and expansion, and it can be shattered by regulating the employed ultrasonic frequency so that it is close to the intrinsic frequency of the rock. The vibration-cutting method was first proposed in the 1960s by Professor Junichiro Kumabe from Utsunomiya University in Japan. A significant number of researchers worldwide have been extensively studying vibration cutting in the machining processes and discovering its excellent process performance for difficult-to-machine materials. Subsequently, attempts are being made to apply vibration

in various other domains. In 2022, scholars from universities and research institutes carried out impact-crushing tests on coal rock and concluded that impact crushing has a significant effect on reducing tool force and specific energy consumption [17]. They also cooperated in completing the development of a vibrating roadheading machine and, after a test, concluded that vibration can reduce the energy consumption of rock-breaking and thus improve the efficiency of rock breaking [18].

Based on vibratory theory testing, Tian et al. [19] proved that high-frequency harmonic vibratory percussion-drilling technology can be used to break rock. Their findings demonstrated that under the excitation of simple harmonic vibration, mechanical drilling speed is increased by approximately 13% in comparison to conventional drilling; the closer the excitation frequency is to the intrinsic frequency of the rock, the greater the mechanical drilling speed, and the greater the rock-breaking efficiency.

Zhang et al. [20] investigated the characteristics of the cyclic excitation of rocks via ultrasonic vibration at a fixed frequency in three stages of progressive damage: 'crack initiation, crack extension and upper end chipping off, cyclic intrusion'. The effectiveness and superiority of the composite action of ultrasonic vibration and 'excitation force + static load force' for rock breaking were clarified.

Yin et al. [21] preliminarily studied the relationship between rock crack formation and strength reduction with respect to ultrasonic vibration and ultrasonic vibration time. In their investigation of the variables influencing the effectiveness of ultrasonic rock breaking.

Pavlovskaia et al. [22] discovered that, within a certain range, the longer the vibration time, the lower the test rock block's uniaxial compressive strength, and the larger the axial pressure, ultrasonic power, and loading area, the shorter the time required for the test rock block to fail.

Li et al. [23] found that the intermediate principal stress direction plays a very important role in inducing the direction of rock crack propagation.

Yang et al. [24] conducted tests on the speed and efficiency of ultrasonic rock breaking and came to the conclusion that ultrasonic high-frequency rotary drilling technology has a rock-breaking efficiency that is nearly 80% higher than that of conventional rotary rock breaking and that the higher the amplitude, the more effective the technology.

Zhao et al. [25] used particle flow discrete element software to simulate the ultrasonic-vibration-assisted hob rock-breaking process. They found that ultrasonic waves contribute to the tensile damage of shallow rock, enhance the scale of crack generation within rock, accelerate the crack generation rate, advance the time of the initial development of cracks, and have a good gain effect on a hob's rock-breaking performance.

Zhao et al. [26] proposed a finite element numerical modeling method for the dynamic cutting process under different ultra-high voltage loads. It was shown that when the excitation frequency was close to the intrinsic frequency of the rock, the mechanical specific energy consumption and cutting force reached the minimum values.

Li et al. [27] modeled rock vibration response with harmonic shock and provided numerical analysis and indoor experimental results. The results confirmed that when the excitation frequency is the same as the intrinsic frequency of the rock, the vibration displacement of the rock is the largest, and the vibration response of the rock increases with the increase in the excitation frequency and shock amplitude and decreases with the increase in the density of the rock.

Huang et al. [28] observed that rock-breaking efficiency increased as the weight on the bit and amplitude increased. They also found that there is an optimal vibration frequency, resulting in the highest rock-breaking efficiency, and the ultrasonic high frequency rotary-percussive drilling technology improved the ROP in deep hard formations via accelerating the fatigue breakdown of hard rocks, reducing the bit's stick–slip vibrations and reasonably utilizing resonance energy.

Li et al. [29] analyzed the crushing mechanism of a rock medium under the condition of simple harmonic vibration and resonance shock. Finite element software was used to analyze the stress state of rock and the axial and torsional motion characteristics of a drill

bit under simple harmonic vibration. The results showed that under simple harmonic vibration impact, rock is more likely to attain tensile strength and accumulate fatigue damage, resulting in crushing; under the impact of resonance, the rock vibration response reaches its peak, which makes it easy to break. Moreover, the impact of simple harmonic vibration can improve the viscosity effect and drilling efficiency of the bit and increase drilling speed.

When the rock-breaking capacity of today's rock-crushing machinery is insufficient, tool wear and tear is severe, and the economic benefits of a task after being affected by such problems are not great, a new solution must be found. However, at the present time, research on ultrasonic vibration rock crushing is still insufficient because the necessary analysis and research methods, means, and resources are severely lacking. There has not been a thorough theoretical investigation of the mechanism by which rocks are destroyed when subjected to ultrasonic vibration; instead, most academics have concentrated on a single aspect, leaving out the influence of other factors on the effectiveness of ultrasonic vibration in breaking rocks. In this paper, we propose an ultrasonically coupled mechanical rock-breaking technology, develop an ultrasonic fracturing simulation method based on test synergy, and conduct research on the fracturing mechanism and properties of ultrasonically pre-crushed rock in order to endow rock-breaking machinery with high efficiency in breaking rock and increase the service life of pick-shaped cut-off teeth. The main contents of this paper consist of four sections: (1) the innovative design of an ultrasonic-coupled mechanical rock-breaking drum, the establishment of the working mechanism of the cooperative drum and the performance of a theoretical analysis of the ultrasonic field in a solid medium, and the development of a clear principle of ultrasonic-coupled mechanical rock breaking; (2) the proposal of an ultrasonic fracturing simulation method based on test synergy, combined with a rock uniaxial compression test and an RFPA^{2D} simulation, to study the effect and mechanism of the ultrasonic pre-crushing fracturing of the target red sandstone; (3) the performance of experimental research on the cracking mechanism of the target red sandstone via ultrasonic pre-crushing based on a nuclear-magnetic-resonance-scanning test and an ultrasonic vibration loading test; and (4) the establishment of a discrete element cutting model (PFC^{2D}) of red sandstone and the comparison of the effectiveness of rock cutting via a pure mechanical single cutter and an ultrasonic-coupled mechanical single cutter to enhance the pre-cracking effect of ultrasonic-coupled mechanical rock breaking.

2. Principle of Ultrasonic-Coupled Mechanical Rock Breaking

A new kind of ultrasonically coupled mechanical rock-breaking drum was creatively designed, as shown in Figure 1, using the mechanical rock-breaking drum of a coal shearer as a prototype. The major component of the ultrasonic pre-fracturing device within this piece of equipment is the center of the end face of the drum. To achieve the objectives of ultrasonic-assisted rock breaking and improved drum cutting performance, a circular array of ultrasonically excited emitters was used to produce axial high-frequency simple harmonic vibrations along the horn. The emitters were in contact with the target rock mass before the drum began picking.

The cone head must extend to the front of the drum, 0.5–1.0 cm beyond the cutting head, and the ultrasonic excitation transmitter head can freely rotate in relation to the horn. The main body of the ultrasonic pre-cracking device rotates synchronously as the new drum operates, breaking the target rock mass. The mechanical arm's thrust is used to move the drum toward the target rock mass and facilitate close contact between the ultrasonic excitation emitter and the rock so that the rock mass can be pre-broken through the ultrasonic vibration energy successfully being transferred to it. The rod-shaped frequency-scanning core is used to excite ultrasonic sounds, receive echo signals from target strata, and provide real-time operating system input on the frequency properties of rock blocks. To allow for adjustment, the ultrasonic excitation transmitter's operating frequency must be similar to or compatible with the natural frequency of the target rock. Keeping the rock block in a state of frequency resonance with the ultrasonic excitation device will also

cause the rock to lose its integrity and some of its strength. Wang et al. [30] considered their proposed approach—in which the robot arm of a shearer was equipped with a nine-axis UR5 robotic manipulator device, which made the shearer more scientifically and reasonably close to the coal wall and thus improved the efficiency of the ultrasonic pre-crushing of coal and rock—feasible, but the findings of this article were not reproducible.
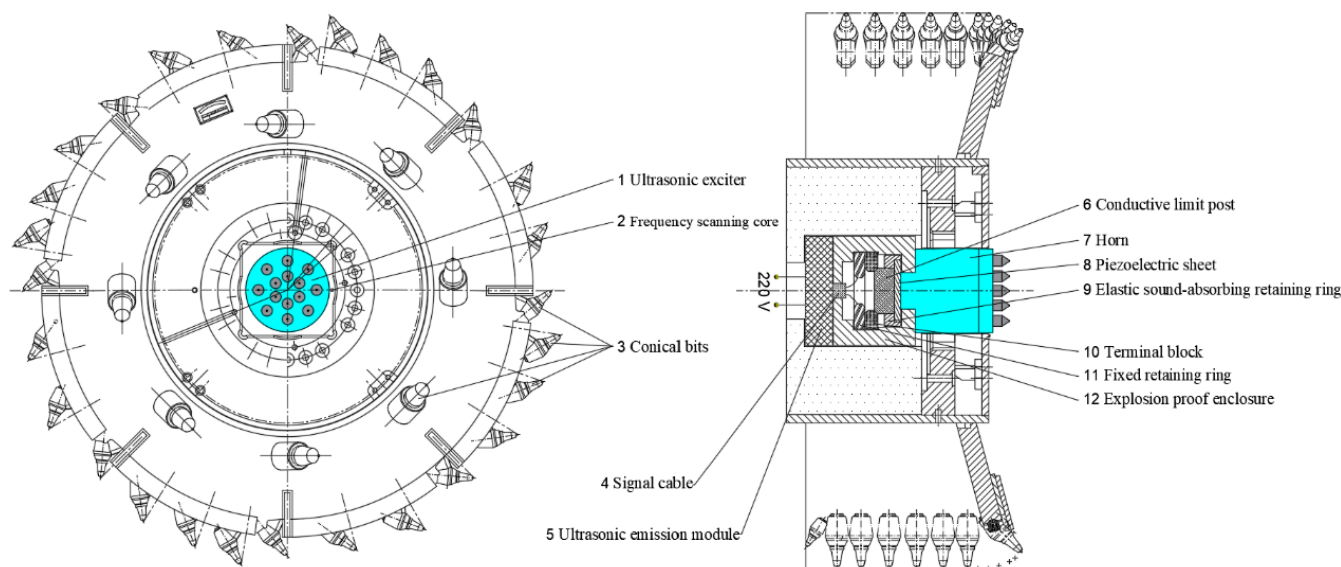

Figure 1. Schematic diagram of ultrasonic-coupled mechanical rock-breaking drum.

The working principle of the new rock-breaking drum (shown in Figure 2) is as follows: (1) By activating the hydraulic adjustment device of the manipulator, the ultrasonic emitter in Figure 2a is effectively attached to the surface of the rock mass at the start of the drum's operation. (2) It is important to note that at this point, the shearer drum does not rotate, and only the initial pre-crushing treatment of the target rock is performed. The ultrasonic cracking device (including the frequency-scanning core) is turned on, the ultrasonic excitation of the rock surface is carried out (as shown in Figure 2b), and the entire shearer is swung synchronously. (3) The entire shearer returns to the working position of the original, regular cutting rock block once the pre-cracking treatment is finished, as indicated in Figure 2c. (4) The shearer drum and the ultrasonic cracking tool are opened simultaneously so that the pick-shaped cutter in Figure 2d can cut the pre-fractured rock block finished in step 2 at the same time that the ultrasonic cracking tool performs pre-cracking on the new rock surface to prepare for the subsequent cutting. (5) Steps 3 and 4 are repeated until the entire rock block has been cut; subsequently, the ultrasonic fracturing device is first switched off, and then the mechanical arm's hydraulic adjusting device's drum is fed in the opposite direction. When the ultrasonic excitation head is not out of alignment with the rock surface, the cutting process is stopped, and the entire shearer device is returned to.

Among the outlined processes, the ultrasonic excitation emitter acting on the rock surface can be equal to the ultrasonic field problem of a circular excitation source radiating in a solid medium, which can be approximated by a uniform isotropic elastic semi-infinite space. The comparable ultrasonic cracking phenomenon may be explained using continuous wave theory and the integral transformation technique when the target rock's free surface is subjected to normal loads that are uniformly distributed throughout the effective region of circular excitation sources. Each field point is situated in the cylindrical coordinate system depicted in Figure 3 because the entire system is axially symmetrically distributed.
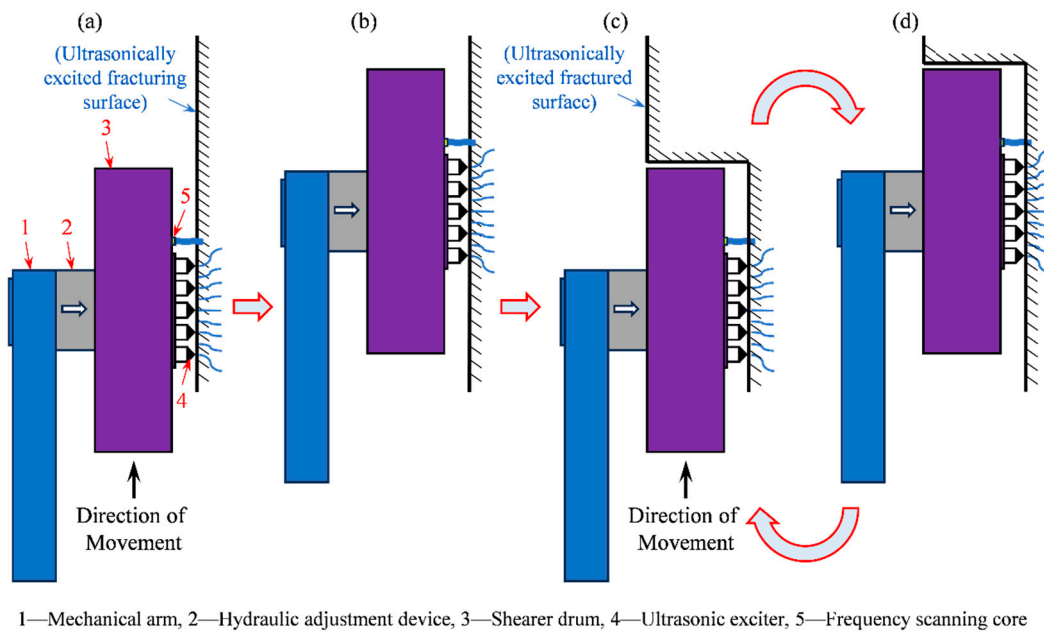
1—Mechanical arm, 2—Hydraulic adjustment device, 3—Shearer drum, 4—Ultrasonic exciter, 5—Frequency scanning core

Figure 2. Working principle diagram of ultrasonic-coupled mechanical rock-breaking drum (black edged arrows represent compressive stress; red edged arrows represent the next step): (**a**) the ultrasonic emitting head is effectively attached to the rock surface and the ultrasonic fracturing device is switched on, (**b**) ultrasonic excitation of the surface of the rock mass (pre-crushing of the rock mass), (**c**) the coal miner is returned to its initial position, ready to start the normal cutting of the rock mass and ready to start the next ultrasonic pre-crushing, and (**d**) end the coal miner's cutting of the rock block at this layer, return and repeat the work of figure (**c**), the coal miner is repositioned to the initial position and the crushing of the rock block at the next layer is carried out until the cutting of the entire target rock block is completed.
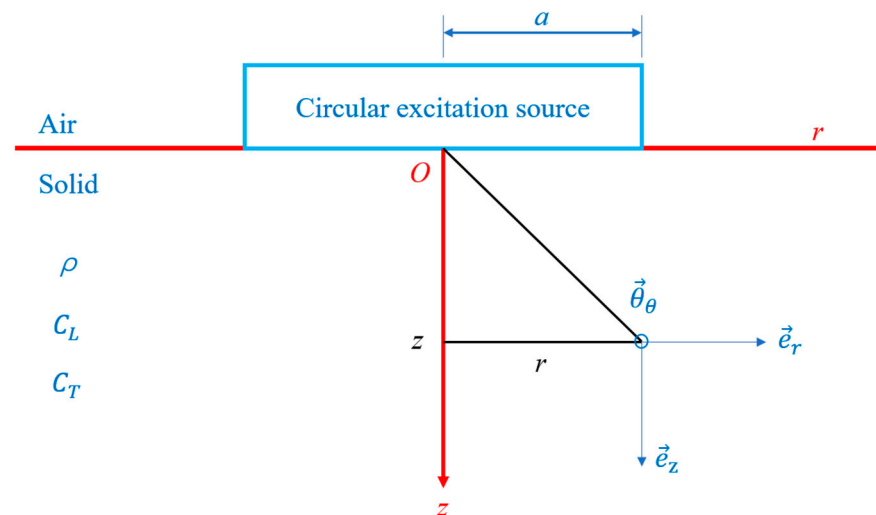

Figure 3. The circular excitation source with radius *a* radiates to a semi-infinite solid medium.

The elastic wave problem in homogeneous and isotropic solid media is usually solved using the vector potential ϕ and scalar potential φ, and the displacement **u** can be expressed as follows:

$$\mathbf{u} = \nabla \varphi + \nabla \times \phi \tag{1}$$

Since the ultrasonic field is symmetrical about the *z*-axis, the displacement **u** has only two components, u_z and u_r, and the vector potential ϕ has only one component, ϕ_θ; for the convenience of expression, ϕ is written instead of ϕ_θ. The variables φ, ϕ, u_z, and u_r only

rely on r, z, and t. Accordingly, the displacement vector Formula (1) can be broken down into

$$u_r(r,z,t) = \frac{\partial \varphi}{\partial r} - \frac{\partial \phi}{\partial z} \tag{2}$$

$$u_z(r,z,t) = \frac{\partial \varphi}{\partial z} + \frac{1}{r} \frac{\partial (r\phi)}{\partial r} \tag{3}$$

The following wave equation is satisfied by the two potential functions

$$\begin{array}{l}
\frac{\partial^2 \varphi}{\partial r^2} + \frac{1}{r} \frac{\partial \varphi}{\partial r} + \frac{\partial^2 \varphi}{\partial z^2} = \frac{1}{c_L^2} \frac{\partial^2 \varphi}{\partial t^2} \\
\frac{\partial^2 \phi}{\partial r^2} + \frac{1}{r} \frac{\partial \phi}{\partial r} - \frac{\phi}{r^2} + \frac{\partial^2 \phi}{\partial z^2} = \frac{1}{c_T^2} \frac{\partial^2 \phi}{\partial t^2}
\end{array} \tag{4}$$

where c_L and c_T are compression wave velocity and shear wave velocity, respectively; λ and μ are *Lame* constants; and ρ is the density of a solid medium. The equations of normal stress σ_{zz} and shear stress σ_{rz} as follows:

$$\begin{array}{l}
\sigma_{zz}(r,z,t) = \frac{\lambda}{c_L^2} \frac{\partial^2 \varphi}{\partial t^2} + 2\mu \left\{ \frac{\partial^2 \varphi}{\partial z^2} - \frac{\partial}{\partial z} \left[\frac{\partial}{r \partial r} \left(r \frac{\partial \phi}{\partial r} \right) \right] \right\} \\
\sigma_{rz}(r,z,t) = \mu \left\{ 2 \frac{\partial^2 \varphi}{\partial r \partial z} + \frac{\partial^3 \phi}{\partial r \partial z^2} - \frac{\partial}{\partial r} \left[\frac{\partial}{r \partial r} \left(r \frac{\partial \phi}{\partial r} \right) \right] \right\}
\end{array} \tag{5}$$

This problem is completely described by initial conditions and boundary conditions. If the semi-infinite space is at rest until $t = 0$, then

$$\begin{array}{l}
\varphi(r,z,0) = \phi(r,z,0) = 0 \\
\frac{\partial \varphi}{\partial t}(r,z,0) = \frac{\partial \phi}{\partial t}(r,z,0) = 0
\end{array} \tag{6}$$

The boundary conditions are

$$\begin{array}{l}
\sigma_{zz}(r,0,t) = \left\{ \begin{array}{ll} f(t), & (r < a) \\ 0, & (r > a) \end{array} \right. \\
\sigma_{rz}(r,0,t) = 0
\end{array} \tag{7}$$

in the equations above, $f(t)$ represents the time variation of the stress exerted by the excitation source on the surface $z = 0$, where a is the radius of the source.

The *Mohr–Coulomb* strength criterion [31] states that when the resultant force of normal stress and shear stress at the point (r, z) reaches the limit stress value of the rock itself, cracks will be generated, and the cracking effect will be achieved.

## 3. Simulation Study on the Cracking Mechanism of Ultrasonic Pre-Crushing

A collaborative experimentally based ultrasonic fracture simulation method is highlighted in this section. It combines a rock uniaxial compression test, an RFPA^{2D} simulation, and an ultrasonic vibration test to sequentially carry out a macro-property test, micro-parameter inversion, ultrasonic fracture simulation analysis, and an ultrasonic fracture experimental study of the target rock in order to reveal the ultrasonic fracture mechanism of the rock.

3.1. Uniaxial Compression Test of Rock

The target red sandstone specimen measures Φ50 × 100 mm and was procured from Laimou Town, Zigong City, Sichuan Province, China. A uniaxial compression test was performed using a TENSON concrete-pressure-testing machine manufactured by Jinan Tianchen Testing Machine Manufacturing Co., Ltd., (Jinan, China), in which the corresponding performance parameters and equipment photos are shown in Table 1 and Figure 4a, respectively. After installing the target red sandstone, as shown in Figure 4b, a typical amount of force was uniformly applied on the horizontal circular cross-section of the cylindrical specimen, and it was gradually loaded at a rate of 0.2 mm/min until the red sandstone was destructed, as displayed in Figure 4c, for which the corresponding uniaxial compressive strength was derived.

Table 1. Compression-test-equipment-related information parameters.

Accurate Measuring Range	Deformation Measurement Accuracy	Test Compression Space	Round Specimen Clamping Diameter	Piston Stroke
20–1000 kN	±0.5% F.S	600 mm	φ 13–φ 60 mm	250 mm

Single-axis compression tester   Red sandstone uniaxial compression test
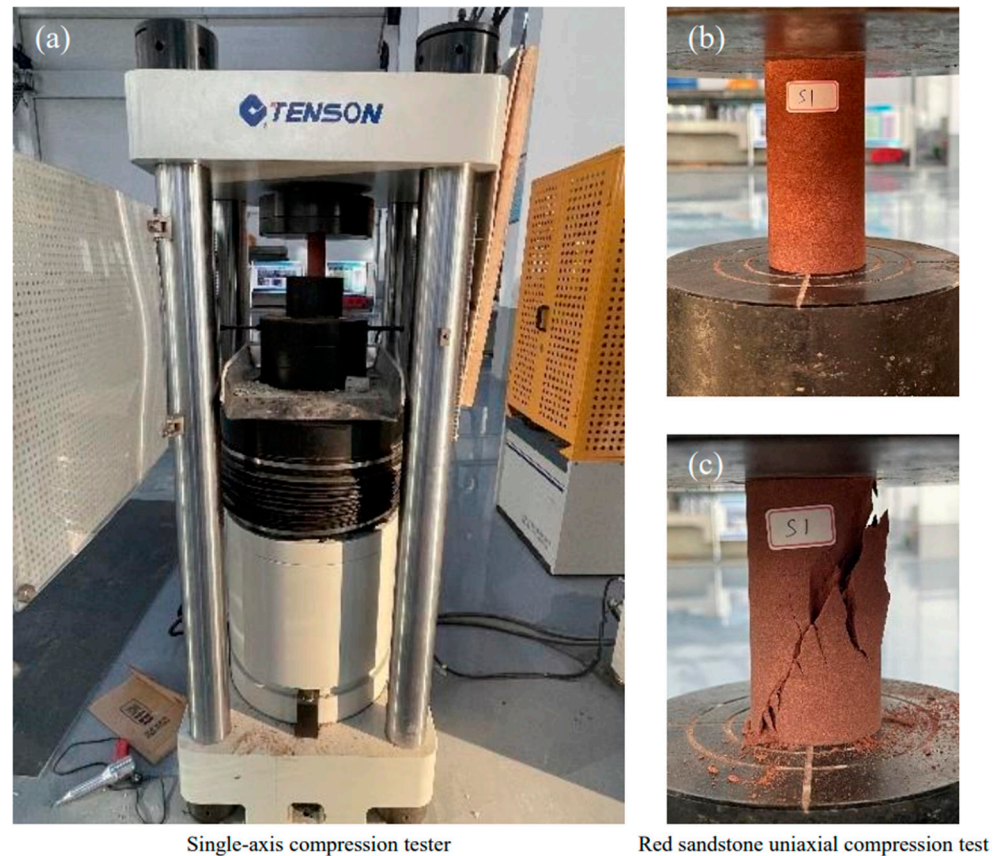
Figure 4. Uniaxial compression test of red sandstone: (**a**) uniaxial compression testing machine with target rock installed, (**b**) rock morphology before the test, and (**c**) rock morphology after the test.

The resulting uniaxial compression strength is

$$\sigma_c = \frac{P}{A_r} \tag{8}$$

where P is the failure load of the sample, and A_r is the cross-sectional area of the sample.

Following the measurement of the samples' axial and transverse strains via the two groups of strain gauges attached to their sides, the elastic modulus and Poisson's ratio of the samples could be calculated as follows:

$$E = \frac{\sigma_{50}}{\varepsilon_{L50}} \tag{9}$$

$$\mu = \frac{\varepsilon_{D50}}{\varepsilon_{L50}} \tag{10}$$

In the equations above, σ_{50} is the stress value (MPa) at 50% uniaxial compressive strength of the specimen, while ε_{D50} and ε_{L50} are the corresponding transverse and longitudinal strain values, respectively.

3.2. Rock Parameter Inversion

In this section, the prerequisites of the collaborative experimentally based ultrasonic fracture simulation method, namely, the inversion of the target rock's measured parameters

using the RFPA^{2D} Rock Fracture Process Analysis System, are described so as to establish an accurate numerical simulation model of the rock and lay the groundwork for the ensuing ultrasonic fracturing simulation analysis. The specific techniques are as follows: (1) Based on the results of the uniaxial compression test conducted on the red sandstone, the values of the fine-scale parameters are preliminarily converted using Equations (11) and (12), while the shear strength and internal friction angle of the rock mass are determined according to the *Mohr–Coulomb* damage criterion, that is, Equations (13) and (14), and then the resulting parameters are used to initially establish the uniaxial compression simulation model (shown in Figure 5). (2) The mesoscale parameter inversion of the target rock was accomplished by using the mesoscale parameters of the numerical simulation model as variables and decreasing the relative error between the red sandstone uniaxial compression test data and the numerical simulation results as inversion objectives. Meanwhile, a comparison of the crushing stress information from the matching computational analysis and experimental testing was conducted, as indicated in Figure 5b.

$$\frac{\sigma_{\text{mac}}}{\sigma_{\text{mic}}} = 0.2602 \ln m + 0.0233 (1.2 \le m \le 50) \tag{11}$$

$$\frac{E_{\text{mac}}}{E_{\text{mic}}} = 0.1412 \ln m + 0.6476 (1.2 \le m \le 10) \tag{12}$$

$$\sigma_\tau = \frac{\sigma_c \sigma_b}{2\sqrt{\sigma_b (\sigma_c - 3\sigma_b)}} \tag{13}$$

$$\tan \varphi = \frac{\sigma_c{}^2 - 4\sigma_\tau{}^2}{4\sigma_c \sigma_\tau} \tag{14}$$

in the equations above, E_{mic} and σ_{mic} represent the fine-scale mean values of the elastic modulus and strength, respectively, at the time of *Weibull* distribution assignment (the numerical calculation input). E_{mac} and σ_{mac} are, in turn, the macroscopic elastic modulus and strength of the numerical specimen. σ_c and σ_b are the macroscopic compressive strength and macroscopic tensile strength of the numerical specimen, respectively, and the unit for both is MPa.
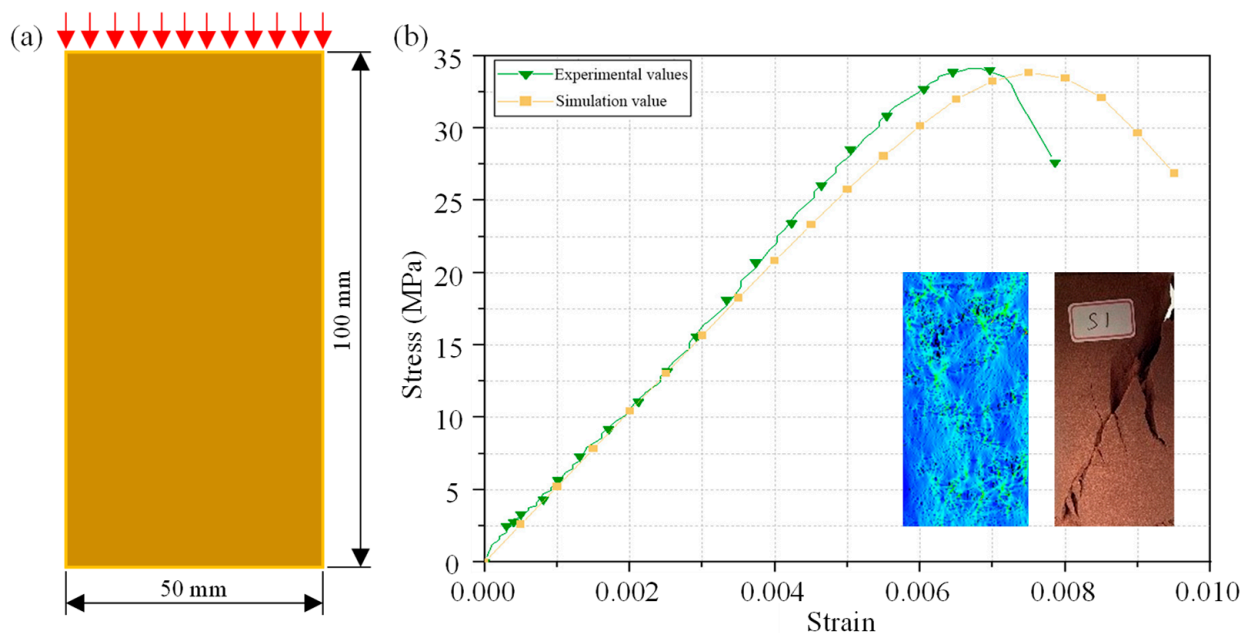

Figure 5. Uniaxial compression of red sandstone: (**a**) red sandstone uniaxial compression simulation model; (**b**) comparison of uniaxial compression simulation and experimental results.

As can be seen from Figure 5b, the uniaxial compression simulation of the red sandstone is highly coincident with the stress–strain curve of the test, and the rock damage

morphology is consistent. Moreover, the limit values of the corresponding uniaxial compressive strengths are 33.8 MPa and 34.1 MPa, respectively, with a relative error of only 0.9%, which indicates that the method has a high degree of accuracy and precision. Furthermore, the inversion parameters of the target red sandstone are shown in Table 2, forming the modeling basis for the subsequent research on the ultrasonic fracturing mechanism.

Table 2. Numerical inversion parameters for red sandstone (RFPA^{2D}).

Target Rock	Parameter	Value
	Elastic modulus (MPa)	5830
	Poisson's ratio	0.248
	Densities (kg/m^3)	2215
Red sandstone	Internal friction angle (°)	60
	Homogeneity coefficient	5
	Uniaxial compressive strength fine average (MPa)	78
	Pressure-to-pull ratio	30

3.3. Simulation and Analysis of Ultrasonic Fracturing Mechanism in Rock

Based on the rock inversion parameters in Table 2, a red sandstone ultrasonic cracking simulation model (RPFA^{2D}) was established, as shown in Figure 6. The model's dimensions are 50 mm × 100 mm, and it is divided into 100 × 200 = 20,000 units. In order to apply harmonic and high-frequency ultrasonic stress loads to the rock blocks for numerical experimental analysis, a dynamic loading method was employed. The corresponding time step is 2.5×10^{-6} s, and there are a total of 100 steps [32]. The waveform of the applied high-frequency vibration is

$$F = A\sin(2\pi f \cdot t) - A \tag{15}$$

where A and f are harmonic amplitude (MPa) and harmonic frequency (Hz), respectively, and t is action duration (s).
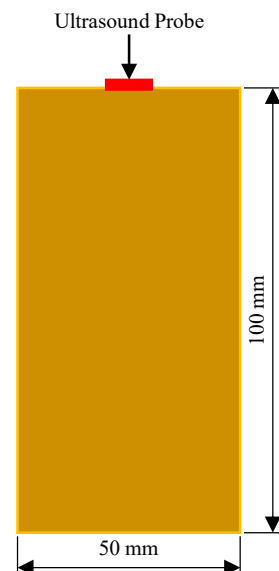

Figure 6. Numerical simulation model of ultrasonic cracking (RPFA^{2D}).

With a fixed harmonic amplitude, namely, $A = 4$ MPa, an excitation force was applied to the upper surface of the RFPA^{2D} model at the frequencies of 20 kHz, 30 kHz, 41 kHz, and 50 kHz to simulate the ultrasonic fracturing phenomenon over 100 iterations, that is, the excitation time $t = 200$ μs. Among these iterations, the rock-fracturing stress patterns for each excitation frequency at the moments of 20 μs, 100 μs, and 200 μs are shown in Figure 7a–d, respectively.
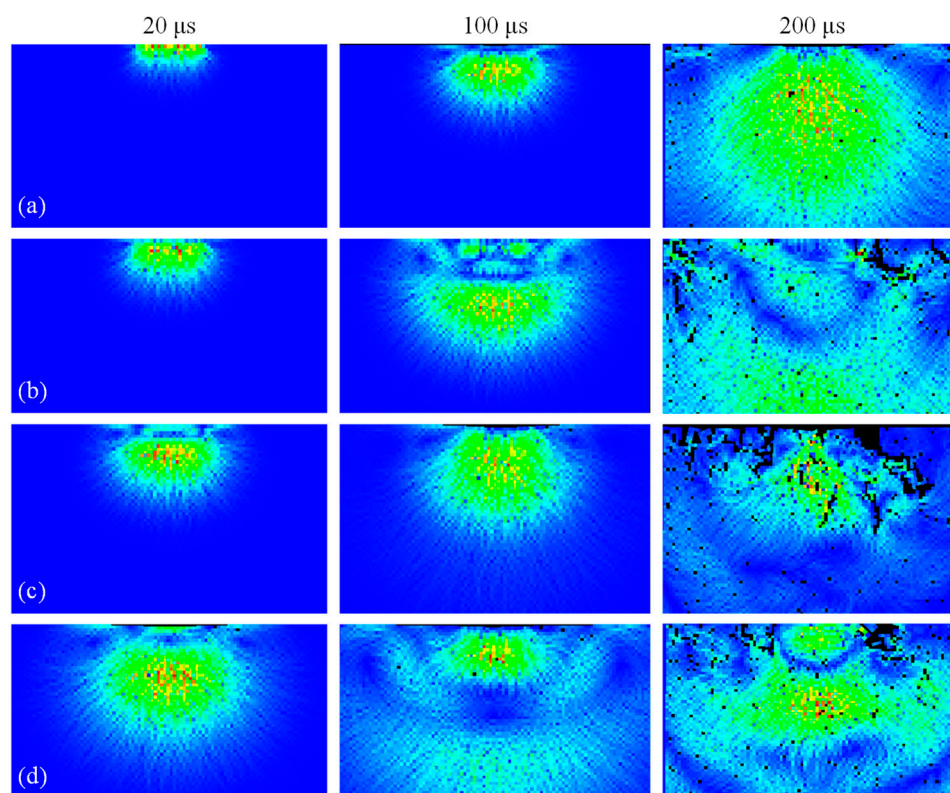
Figure 7. Rock fracturing at different frequencies for ultrasonic excitation with a fixed amplitude of 4 MPa (the change in module colour from blue, to green, to yellow, to orange and finally to red, corresponds to a gradual increase in the value of the stresses applied to the internal units of the module): (**a**) 20 kHz, (**b**) 30 kHz, (**c**) 41 kHz, and (**d**) 50 kHz.

As can be seen from the stress clouds propagated by the ultrasonic vibrations in the simulation module in Figure 7, the high-stress regions usually appear as a saturated bright-red color and are present in the center of each cycle of the vibration waveform, indicating that this region receives a higher level of stress, and this region is usually the first to develop cracks. A trumpet-shaped waveform contour area can be seen throughout the stress cloud; this is the propagation path of the ultrasound in the rock model, indicating that the stress spreads along the path as the ultrasound is conducted through the rock. The formation and expansion of cracks in the rock model can be seen in the stress cloud map, where cracks are indicated by dark-black areas, and with the action of ultrasound, the cracks will start to sprout from the high-stress areas and gradually expand to the surrounding low-stress areas. The maximum degree of cracking at 41 kHz can be clearly distinguished from the stress cloud. By observing the stress maps of the ultrasonically fractured rocks, we can obtain a visual representation of the stress distribution inside the rocks, and then we can use the acoustic emission analysis module of the RFPA^{2D} software (Basic 1.0) to export the acoustic emission data and then compare and analyze the acoustic emission data quantitatively through Figure 8.

From the above figure, it can be seen that the cumulative amount of acoustic emission is 68 at 20 kHz, 272 at 30 kHz, 513 at 41 kHz, and 337 at 50 kHz, and the simulation simulates the same time step with the highest cumulative amount of acoustic emission and the optimal fracturing effect of the red sandstone at a frequency of 41 kHz. A comparison of the fracturing morphology of the red sandstone simulated in the simulation also shows that after running all the time steps at 41 kHz (the total time step is 100 steps, that is, 200 μs), the degree of internal fracturing of the red sandstone is greater than in the other cases.
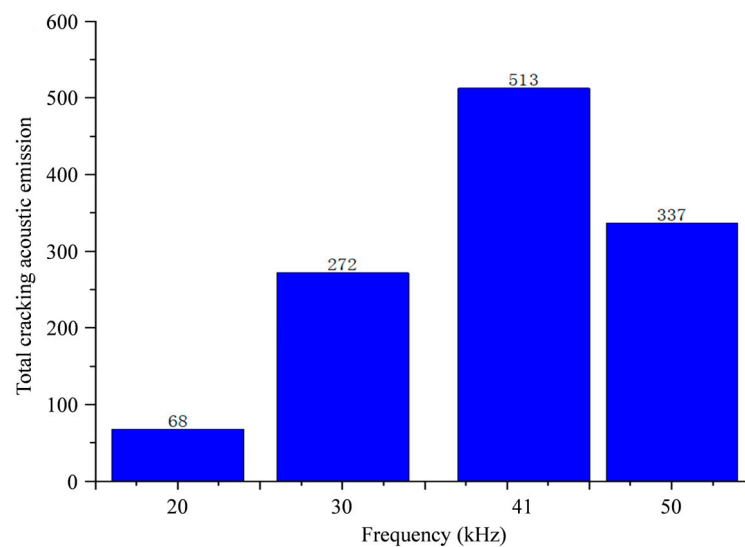
Figure 8. Comparison of total fractured acoustic emissions from red sandstone.

In turn, for a fixed harmonic frequency f = 41 kHz (this optimum vibration frequency has been derived from the above), the excitation force is applied to the upper surface of the RFPA^{2D} model at the amplitudes of 2 MPa, 3 MPa, 4 MPa, and 5 MPa to simulate the ultrasonic fracturing phenomenon over 100 iterations, that is, the excitation time t = 200 μs. Among them, the rock-fracturing stress patterns for each vibration amplitude at the moments of 20 μs, 100 μs, and 200 μs are shown in Figure 9a–d, respectively.
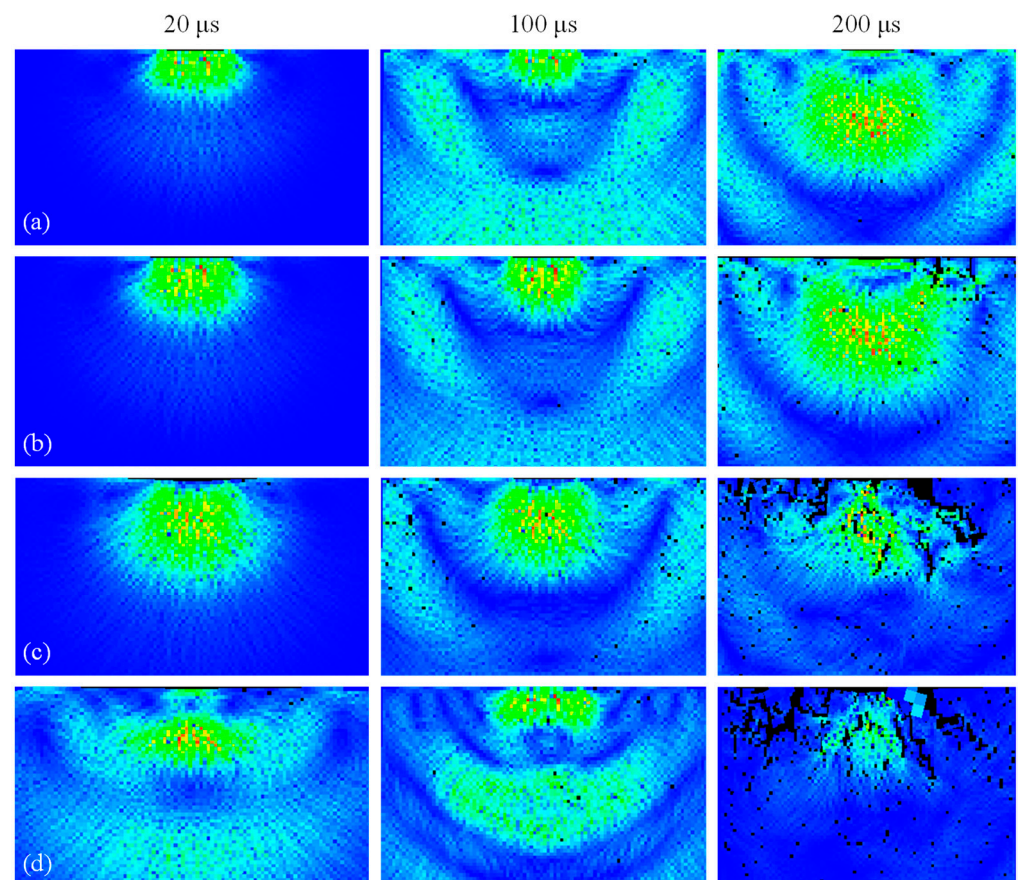
Figure 9. A 41 kHz comparison of cracking at different amplitudes: (**a**) 2 MPa, (**b**) 3 MPa, (**c**) 4 MPa, and (**d**) 5 MPa.

In the stress maps of ultrasonic vibration propagated in the simulation module in Figure 9, it can be seen that the degree of fracturing at amplitudes of 4 MPa and 5 MPa is much larger than that at 2 MPa and 3 MPa, and the degree of fracturing at amplitudes of 4 MPa and 5 MPa is about the same. By observing the stress maps of ultrasonically fractured rocks, we can obtain a visual representation of the stress distribution inside the rocks, and then we can use the acoustic emission analysis module of RFPA^{2D} software (Basic 1.0) to export the acoustic emission data and analyze the acoustic emission data quantitatively through the comparison in Figure 10.
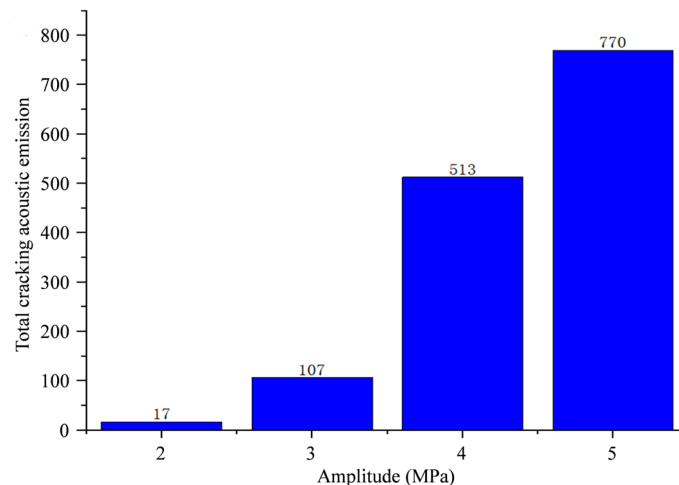
Figure 10. Comparison of total fractured acoustic emission from red sandstone.

As can be seen in the above figure, the cumulative amount of acoustic emission is 17 at 2 MPa, 107 at 3 MPa, 513 at 4 MPa, and 770 at 5 MPa. Obviously, at the amplitude of 5 MPa, the simulation has the greatest cumulative amount of acoustic emission for the same time step, and the fracturing effect is optimal for red sandstone. However, the rate of increase in acoustic emission accumulation with time step at 4 MPa is more drastic than that at 2 MPa, 3 MPa, and 5 MPa, and it is easy to realize an amplitude of loading equal to 4 MPa in practical tests, so 4 MPa was considered the optimum amplitude for the overall situation.

In Figure 11 below, the damage model for red sandstone under sinusoidal excitation at a frequency of 41 kHz and an amplitude of 4.0 MPa is depicted.
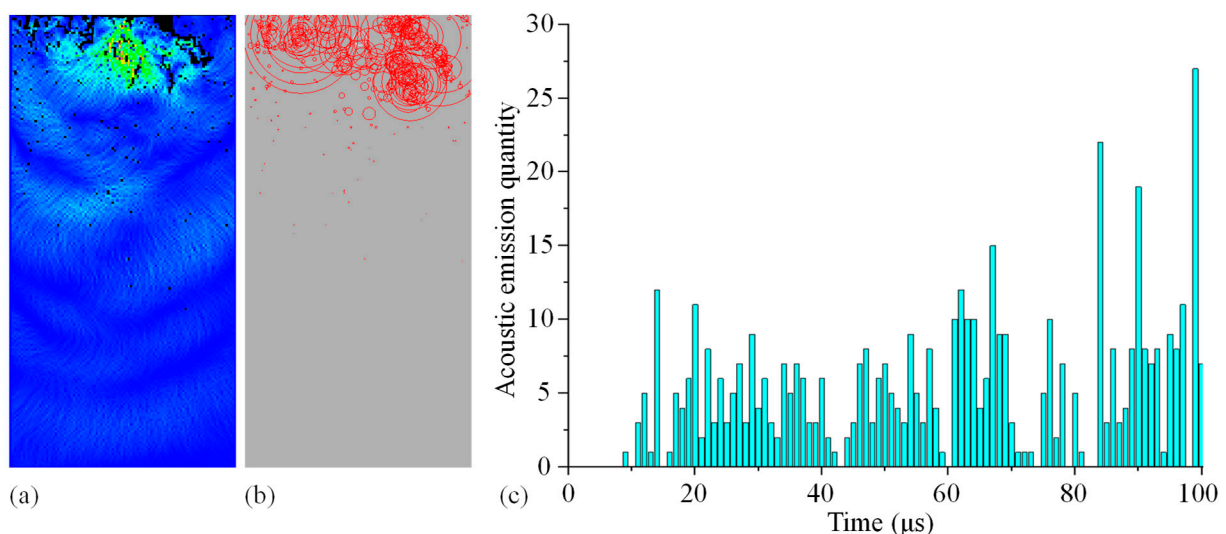

Figure 11. Ultrasonic simulation fracturing of red sandstone (sinusoidal excitation frequency—41 kHz; amplitude—4.0 MPa): (**a**) Fracture map of red sandstone, (**b**) acoustic emission map of fractured red sandstone, and (**c**) red sandstone acoustic emission frequency.

The size of the circles symbolizes the amount of energy produced when the unit is damaged, and the red circles denote tensile damage, while the white circles indicate shear damage [33]. In the cracking acoustic emission diagram, it can be seen that rock cracking has been achieved at this time. In addition, from the acoustic emission comparison results, it can be concluded that the rock-breaking effect is best at the frequency corresponding to the simulation in Figure 11. The simulation of the red sandstone produces 513 micro-cracks, from which it can be gleaned that ultrasound in a certain range of frequencies can effectively induce a number of cracks in the internal rock block, reduce the strength of the rock block, and loosen the internal structure, allowing the subsequent pick-axe-shaped tooth cutting breakage process to provide a good environment for the improvement of the tooth-tip wear-resistance cycle to prevent these teeth from constantly being subjected to excessive stress that shortens the service life of the truncated teeth.

Figure 11 depicts the fracturing simulation pattern when the ideal frequency and amplitude are used (41 kHz, 4 MPa). The fracturing mechanism is resonant rock fragmentation, and the resonance principle can be utilized to explain the rock's fracturing. Resonance is defined as a ratio of 0.75 to 1.25 between the excitation frequency and the intrinsic frequency of the target rock mass, causing the object's amplitude at a specific location to increase over time with the goal of crushing the rock body. If a simple harmonic vibration source with a high frequency continues to excite rock, this will result in a comparable response. This is because the vibration is being forced, and this force is a simple harmonic excitation force. Figure 12 below depicts the simplified model's operating principle.
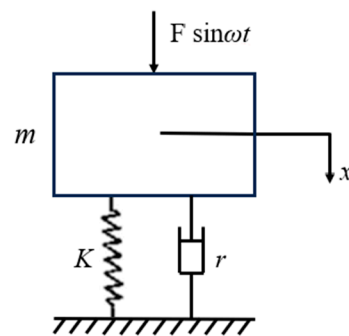

Figure 12. Forced vibration working principle diagram.

Then, the displacement response, that is, amplitude *B*, produced by the rock is

$$B = \frac{F/K}{\sqrt{(1-\lambda^2)^2 + (2\xi\lambda)^2}} \tag{16}$$

where *K* is the stiffness coefficient of rock, λ is the frequency ratio (the ratio of external excitation frequency to rock intrinsic frequency), and ξ is the relative damping factor.

In actual rock breaking, the relative damping coefficient of rock is very small, i.e., approximately equal to the value of 0. Therefore, from Equation (16) above, it can be deduced that when $\lambda \approx 1$, the denominator tends to the value of 0, and then the amplitude *B* tends to the maximum value, so the rock-fracturing effect is optimal in this case. So far, the theory proves why the simulated fracturing effect of the rock mass is optimal when the value of the external excitation frequency is approximately equal to the value of the intrinsic frequency of the target rock.

4. Experimental Research on Ultrasonic Pre-Crushing Fracturing Mechanism

In this section, the change in the porosity of the target red sandstone before and after ultrasonic vibration was experimentally measured to reveal the ultrasonic pre-fracturing mechanism. This experiment consists of two components: a nuclear magnetic resonance (NMR) scanning test and an ultrasonic vibration loading test. It is important to note that

porosity, also known as rock porosity, is the ratio of the total volume of all pore spaces in a rock sample to the volume of that rock sample, represented as a percentage.

4.1. NMR Test before Vibration

For the NMR experiment before vibration, the core components of the test setup were an NMR analyzer and an evacuation vacuum pressurization saturation device, models MesoMR23-060H-I and BH-II, respectively, as shown in Figure 13. The corresponding working parameters are shown in Tables 3 and 4, respectively. It is worth emphasizing that the evacuation vacuum pressurization saturation device mainly consists of a core chamber, a vacuum pump, and a pressurization device.

Figure 13. NMR experimental setup: (**a**) NMR scanner; (**b**) model BH-II rock core evacuation vacuum pressurization saturation device.

Table 3. Working parameters of nuclear magnetic resonance scanning device.

Main Magnetic Field (T)	Main Frequency (MHz)	Pulse Frequency (MHz)	Gradient Field (T/m)	Magnetic Field Stability (Hz/h)	Magnet Temperature (°C)	Magnet Uniformity (ppm)
0.52 ± 0.05	21.3	1~49.9	0.03	<300	25~35	20

Table 4. Operating parameters of vacuum saturation device.

Core Chamber Size (mm)	Vacuum Pressure Range (MPa)	Full Water Pressure Range (MHz)
Φ 120 × 400	0~−0.1	0~60

The target red sandstone sample was prepared by saturating it with water prior to NMR testing to determine its initial porosity. The findings of the initial water saturation treatment and NMR test performed on the standard specimen of red sandstone with dimensions of φ 40 × 80 mm are displayed in Figure 14. As seen in the figure, the initial porosity of the red sandstone specimen is 12.51%, and the pore throat radius of the pores is primarily dispersed in the range of 0~0.1 μm.
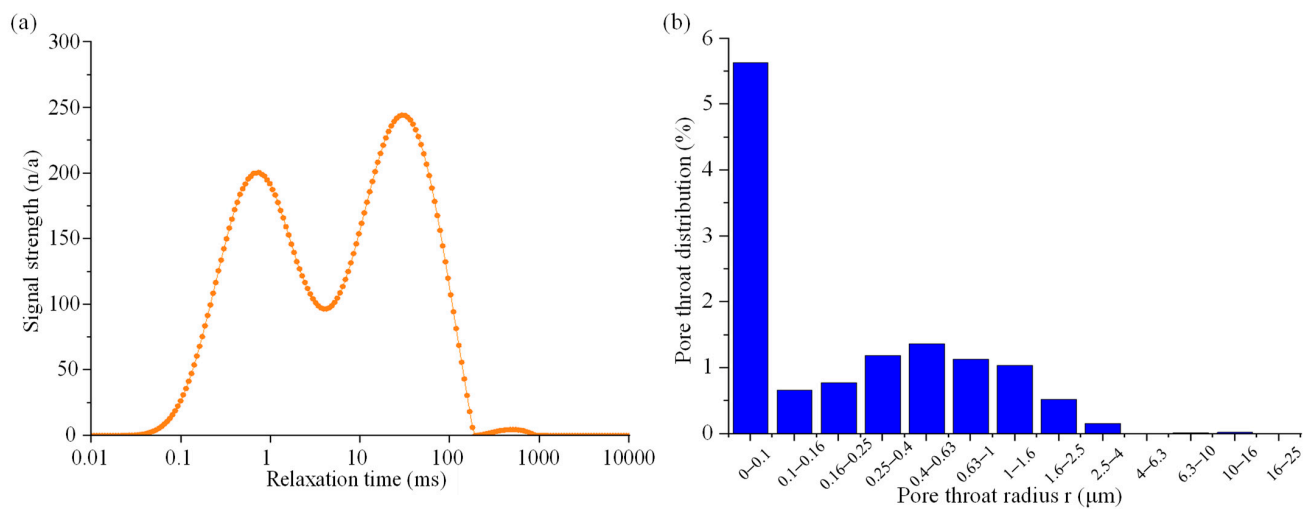
Figure 14. Magnetic resonance imaging (MRI) scanning test before vibration: (**a**) vibration signal strength; (**b**) pore throat distribution in target red sandstone.

4.2. Ultrasonic Cracking Test

The ultrasonic vibratory rock-breaking device presented in Figure 15 was the key to performing the ultrasonic fracturing test, the core component of which is an ultrasonic transducer, which produces ultrasonic vibrations by means of a variable-amplitude rod. The ultrasonic transducer consists of a variable-amplitude rod, a piezoelectric ceramic sheet, an upper end cap, and a lower end cap, and the corresponding working principle is as follows: the use of piezoelectric ceramics with an inverse piezoelectric effect, under the action of the drive power supply that produces high-frequency longitudinal vibrations, via the variable-amplitude rod will be the amplitude of the high-frequency longitudinal vibration amplitude for amplification and output.
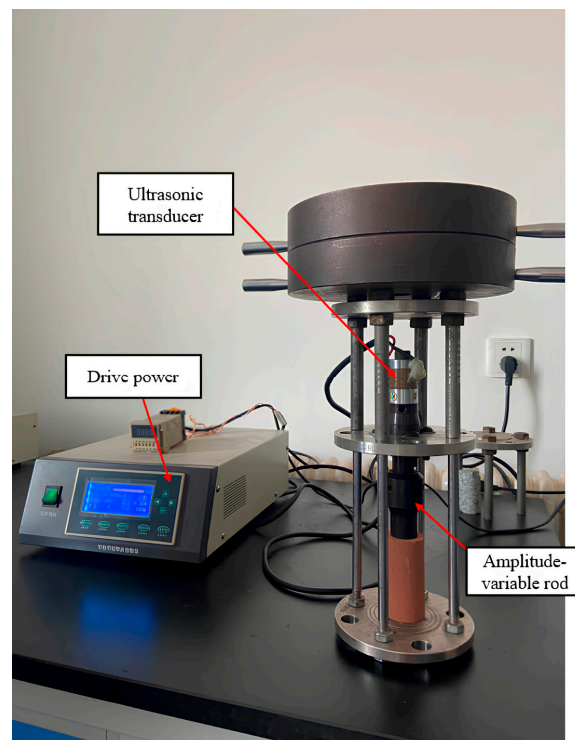
Figure 15. Ultrasonic vibration device.

The target red sandstone sample yielding results consistent with the NMR test before vibration was mounted on the ultrasonic vibration device, and an ultrasonic cracking test was conducted in accordance with the precise loading procedure in Table 5; then, the saturation treatment and NMR tests were carried out sequentially after vibration, with the results shown in Figure 16. It is obvious that the pore throat distributions of the target red sandstone samples before and after ultrasonic vibration are highly similar, with a porosity of 15.04% after vibration, and the corresponding changes in porosity are listed in Table 6.

Table 5. Ultrasonic vibratory loading program.

Sample Material	Pre-Stressing	Loading Frequency	Loading Amplitude	Loading Time
Red sandstone	200 N	40 kHz	40 μm	20 s

(a)

(b)
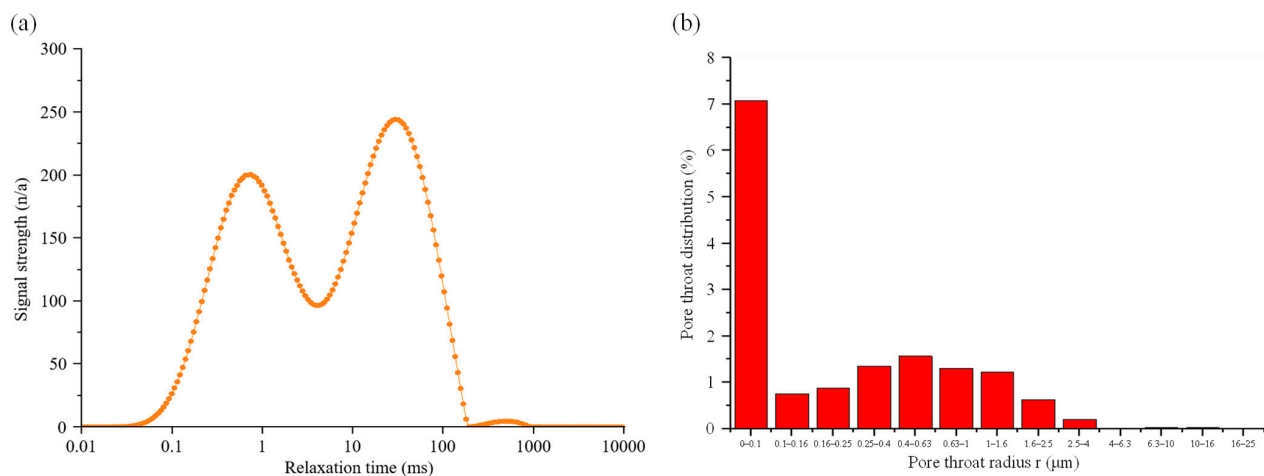
Figure 16. MRI scanning test after vibration: (**a**) vibration signal strength; (**b**) pore throat distribution in target red sandstone.

Table 6. Changes in porosity of red sandstone sample.

Red Sandstone Sample	Vibration Duration (s)	Initial Porosity (%)	Post-Vibration Porosity (%)	Porosity Change (%)	Porosity Change Rate (%)
	20	12.51	15.04	2.53	20.2238

As can be seen in Table 6, the porosity change rate between the red sandstone sample before and after ultrasonic vibration reached as high as 20.2238%. Ultrasonic vibration obviously increases the porosity of the rock while decreasing its strength, and as the vibration time increases, the cracking effect becomes increasingly noticeable.

To investigate the effect of ultrasonic vibration on the pore size within the target red sandstone, the distribution of pore throat radii before and after vibration was comparatively analyzed, as shown in Figure 17. It is clear that after the ultrasonic vibratory loading of the rock samples, the pore throat distributions in different pore throat radius intervals were all higher than those before ultrasonic vibratory loading. The results indicate that the pores and cracks of the rock samples after ultrasonic vibration gradually developed and expanded, resulting in the gradual enlargement of the original small pores and the concomitant generation of new pores.
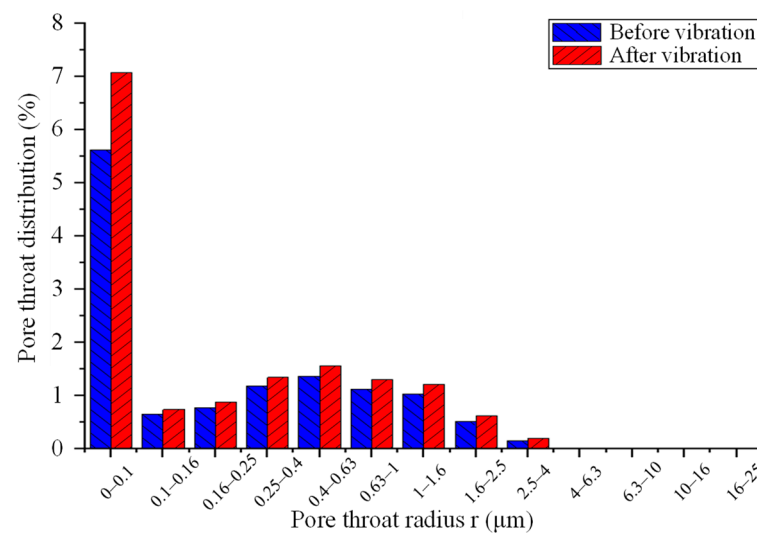
Figure 17. Pore throat distributions of red sandstone sample before and after ultrasonic vibration loading.

In addition, the fracture simulation model (RPFA^{2D}) of red sandstone under ultrasonic vibration excitation with a frequency of 40 kHz and an amplitude of 2.1 MPa was established. It is worth pointing out that the excitation amplitude of 2.1 MPa was calculated via analogy with the stress–strain curve of the uniaxial compression test of red sandstone; thus, the ultrasonic load applied by this simulation was $F = 2.1 \times \sin(80{,}000\pi \cdot t) - 2.1$ (unit: MPa). The fracture morphology, acoustic emission map, and acoustic emission accumulation of the red gauze rock were numerically analyzed, as shown in Figure 18.
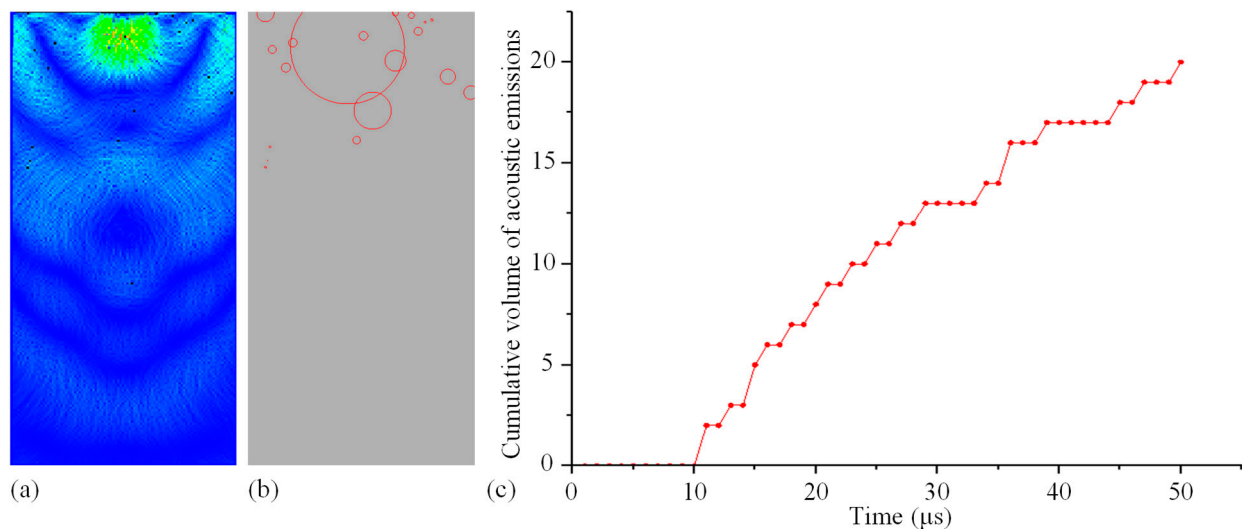
Figure 18. Simulation of red sandstone fracturing under ultrasound at 40 kHz and 2.1 MPa: (**a**) fracture pattern diagram, (**b**) cracking acoustic emission tomography, and (**c**) cumulative volume of acoustic emissions.

As observed in the above graphic, red sandstone can be effectively fractured via ultrasonic high-frequency vibration. In actual experiments, there is an increased distribution of pore throats within the red sandstone and an increase in porosity. In simulated experiments, there is an accumulation of acoustic emissions, and this is consistent with the results of the actual experiments. These results demonstrate the excellent fracturing effect of ultrasound.

5. Study on the Pre-Fracturing Effect of Ultrasonically Coupled Mechanical Rock-Breaking

In this section, the focus is on comparing the rock-breaking capabilities of the mechanical and ultrasonic-coupled single-tooth truncation methods, and PFC^{2D} was used to perform a discrete elemental simulation of the truncated red sandstone in order to thoroughly investigate the pre-fracturing effect of the latter. First, a parametric inversion of the target red sandstone was carried out—according to a principle similar to the methodology provided in Section 3.2, which will not be repeated here—to determine the physical parameters of the red sandstone that match the discrete meta-cutoff model (PFC^{2D}) of the red sandstone (see Table 7). Then, a cutting model with dimensions of 250 × 120 mm was established, and the rock-cutting processes of purely mechanical single-gear and ultrasonic-coupled mechanical single-gear devices were simulated successively. The corresponding rock-breaking effects are shown in Figures 19 and 20, respectively.

Table 7. Inversion parameters of the discrete element cutting model for red sandstone (PFC^{2D}).

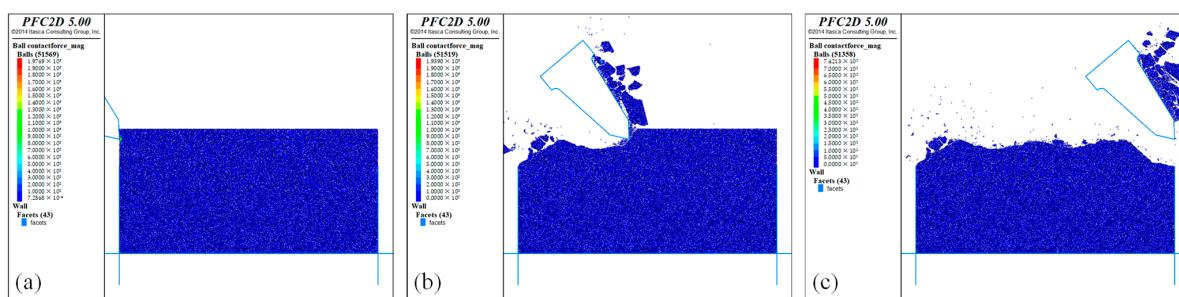| Target Rock	Parameter	Value
Red sandstone	Modulus of elasticity of bond (MPa)	2200
	Bond stiffness ratio	2.1
	Bonding tensile strength (MPa)	6.0
	Bond strength ratio	2.0
	Poisson's ratio	0.25
	Particle friction angle (°)	64

Figure 19. Purely mechanical single-cut-off tooth device's cutting and breaking effects: (**a**) start of cutting, (**b**) in the process of cutting, and (**c**) at the end of cutting.

As seen in Figures 19 and 20, the ultrasonic-coupled-mechanical-single-tooth-cut rock has much better stability and debris refinement than the pure-mechanical-single-gear-cut rock. The pure-mechanical-single-gear-cut rock had much less flying debris and much less rock block damage than the ultrasonic-coupled-mechanical-single-gear-cut rock. At the same time, the combined force of the cutting heads during the motion of the cutting teeth in the aforementioned cutting model (as illustrated in Figure 21) was compared and examined in order to better describe the pre-cracking effect of ultrasonically linked mechanical rock breaking. As can be observed, pure mechanical rock breaking resulted in an instantaneous impact force of the cutting head that was substantially larger than that produced via ultrasonically linked mechanical rock breaking, the latter of which is better for extending the life of the cutting teeth. The average cutting force for pure mechanical cutting was 6374 N, while the average cutting force for ultrasonic-coupled rock breaking was 4185 N. In pure mechanical rock breaking, the pick's average cutting force is also greater than that in ultrasonically linked rock breaking. It can be argued that ultrasound can loosen the structure of the rock, making mechanical rock cutting simpler.
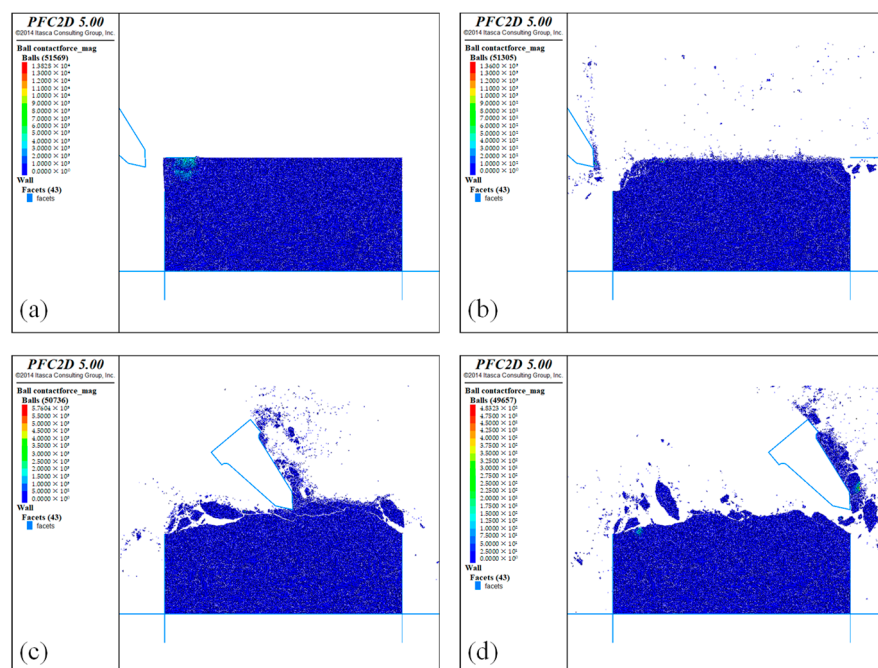
Figure 20. Ultrasonic-coupled mechanical single-cut-off tooth device's cutting rock-breaking effect: (**a**) the start of ultrasonic pre-cracking, (**b**) the end of ultrasonic pre-cracking, (**c**) in the cutting process, and (**d**) the end of cutting.
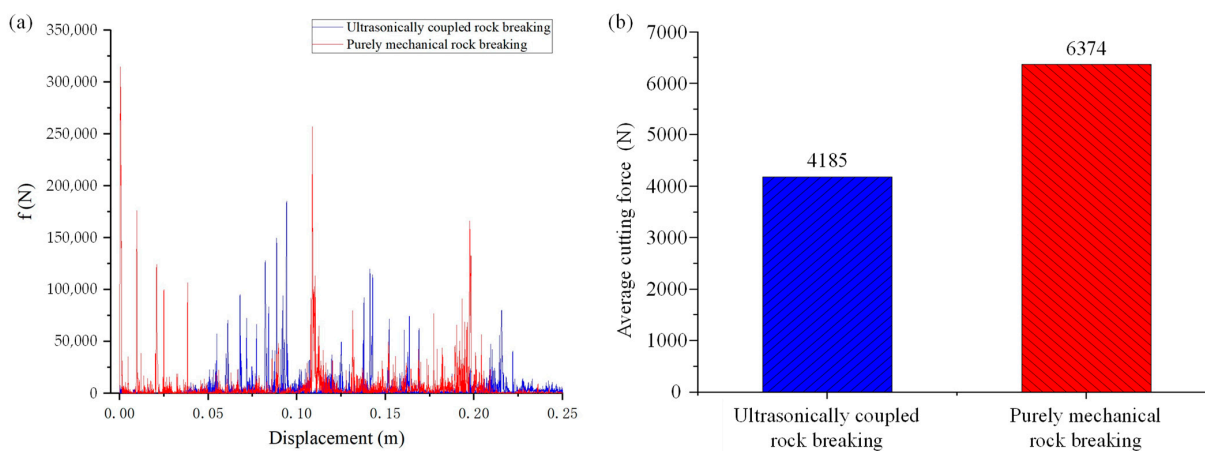

Figure 21. Analytical diagram of the combined force acting on the cutting tooth during movement: (**a**) cutting head instantaneous force diagram; (**b**) comparison of mean cutting forces between ultrasonic coupling and pure machinery.

6. Conclusions

Aiming to address the major problem of how to break rocks efficiently and quickly faced by the mining industry, in this study, we proposed an ultrasonic-coupled mechanical rock-breaking technology, developed an ultrasonic fracturing simulation method based on test synergy, and carried out research on the fracturing mechanism and characteristics of ultrasonically pre-broken rocks. The following four elements make up the primary research content: First, we designed an innovative ultrasonic-coupled mechanical rock-breaking drum, analyzed the ultrasonic propagation mechanism in a semi-infinite medium, carried out an ultrasonic fracture determination of the target rock body with the help of the *Mohr–Coulomb* strength criterion, and theoretically revealed the ultrasonically coupled rock-breaking mechanism. Second, combined with a rock uniaxial compression test and an RFPA^{2D} simulation, an ultrasonic-coupled mechanical rock-breaking technology was

proposed to study the effect and mechanism of the ultrasonic pre-crushing fracturing of the target red sandstone. Third, an experimental study on the mechanism of the ultrasonic pre-crushing and fracturing of the target red sandstone, consisting of a nuclear magnetic resonance scanning test and an ultrasonic vibration loading test, was carried out to further clarify the mechanism of the ultrasonic fracturing effect. Finally, the ultrasonic-coupled mechanical rock-breaking technology's pre-crushing effect was further investigated through an effectiveness comparison, carried out using a red sandstone discrete element cutting model (PFC^{2D}), for pure mechanical single-cut teeth and single-cut teeth. The results show that ultrasonic pre-crushing in a specific frequency range effectively induced internal micro-cracks in the rock block, reduced the strength of the rock block, and disintegrated its internal structure. Additionally, ultrasonic micro-vibration is not enough to cause large vibrations of the shearer swing arm, which will not reduce the overall stability and reliability of the shearer and, to a certain extent, can stave off the pick-shaped teeth assuming a state of high stress during cutting for a long time, and it can slow down the failure period of the friction damage of the tooth tip and extend the working life of the pick. The following are the main conclusions:

(1) The best cracking impact of an ultrasonic wave was at the corresponding frequency of 41 kHz, where the acoustic emission accumulation was the largest, reaching 513.

(2) The initial porosity of the red sandstone samples was 12.51%, and the porosity after the application of ultrasonic vibration was 15.04%, with the amount of change in porosity amounting to 2.53% and the rate of change in porosity equaling 20.2238%. The pore volume ratios of the rock samples in different pore-throat radius intervals after ultrasonic vibratory loading were higher than those before ultrasonic vibratory loading. After ultrasonic vibration, the pores and cracks of the rock samples gradually developed and expanded, resulting in the originally small pores gradually becoming larger, accompanied by the generation of new pores, and the ultrasonic waves applied with the intrinsic frequency of the rock caused cracking inside the rock and expanded the size of the pores.

(3) The pure mechanical average cutting force was 6374 N, while the ultrasonic-coupled breaking average cutting force was 4185 N, which is 34.34% lower, and this can be attributed to the loose rock structure induced by the ultrasonic wave. Not only can this coupled rock-breaking technology easily break rock via mechanical cutting, but the lower force applied can also shorten the wear failure period of pickaxe teeth.

(4) The proposed collaborative experimentally based ultrasonic fracture simulation method has high accuracy and reliability, which are conducive to promoting the development of new rock-breaking technology.

References

1. Wang, G.F.; Xu, Y.X.; Ren, H.W. Intelligent and ecological coal mining as well as clean utilization technology in China: Review and prospects. *Int. J. Min. Sci. Technol.* **2019**, *29*, 161–169. [CrossRef]
2. Eshaghian, O.; Hoseinie, S.H.; Maleki, A. Multi-attribute failure analysis of coal cutting picks on longwall shearer machine. *Eng. Fail. Anal.* **2021**, *120*, 105069. [CrossRef]
3. Xu, P.; Yang, R.; Zuo, J.; Ding, C.; Chen, C.; Guo, Y.; Fang, S.; Zhang, Y. Research progress of the fundamental theory and technology of rock blasting. *Int. J. Miner. Metall. Mater.* **2022**, *29*, 705–716. [CrossRef]
4. Li, H.; Wang, J.; Mei, Q.; Huang, K.; Luo, Q.; Dong, J. Numerical Simulations and Experiments on Single-Tooth Rock-Breaking. *Machines* **2022**, *10*, 455. [CrossRef]
5. Hassani, F.; Nekoovaght, P. the development of microwave assisted machineries to break hard rocks. *ISARC* **2011**, *2*, 72–78.
6. Guo, C.G.; Sun, Y.; Yue, H.T.; Li, Q.; He, S.Z.; Zhang, J.Z.; Zhang, Y. Experimental research on laser thermal rock breaking and optimization of the process parameters. *Int. J. Rock. Mech. Min. Sci.* **2022**, *160*, 105251. [CrossRef]
7. Zheng, Y.L.; He, L. TBM tunneling in extremely hard and abrasive rocks: Problems, solutions and assisting methods. *J. Cent. South Univ.* **2021**, *28*, 454–480. [CrossRef]
8. Gwarek, W.K.; Celuch-Marcysiak, M. A review of microwave power applications in industry and research. *IEEE Cat. No.04EX824.* **2004**, *3*, 843–848.
9. Gao, M.Z.; Yang, B.G.; Xie, J.; Ye, S.Q.; Liu, J.J.; Liu, Y.T.; Tang, R.F.; Hao, H.C.; Wang, X.; Wen, X.Y.; et al. The mechanism of microwave rock breaking and its potential application to rock-breaking technology in drilling. *Pet. Sci.* **2022**, *19*, 1110–1124. [CrossRef]
10. Osepchuk, J.M. A History of Microwave Heating Applications. *IEEE Trans. Microw. Theory Tech.* **1984**, *32*, 1200–1224. [CrossRef]
11. Jones, D.A.; Kingman, S.W.; Whittles, D.N. Understanding microwave assisted breakage. *Miner. Eng.* **2005**, *18*, 659–669. [CrossRef]
12. Clark, D.E.; Sutton, W.H. Microwave Processing of Materials. *Annu. Rev. Mater. Sci.* **1996**, *26*, 299–331. [CrossRef]
13. Han, W.F. Experimental Study on Rock-Breaking Using a Water Jet Assisted Mechanical Disc Cutter. *Tunn. Constr.* **2022**, *42*, 1414–1419.
14. Li, X.H.; Wang, J.S.; Lu, Y.Y.; Yang, L.; Kang, H.M.; Sun, J.J. Experimental investigation of hard rock cutting with collimated abrasive water jets. *Int. J. Rock Mech. Min. Sci.* **2000**, *37*, 1143–1148.
15. Fan, C.X.; Zhang, H.T.; Kang, Y.; Shi, H.Q.; Li, D. Rock breaking performance of the newly proposed unsubmerged cavitating abrasive waterjet. *Int. J. Min. Sci. Technol.* **2023**, *33*, 843–853. [CrossRef]
16. Liu, L.S.; Zhao, D.J. Effects of the Ultrasonic Vibration Frequency on the Rules of Rock Crushing. *Solid State Technol.* **2020**, *29*, 2174–2179.
17. Wang, S.F.; Sun, L.C.; Tang, Y.; Jing, Y.; Li, X.B.; Yao, J.R. Field application of non-blasting mechanized mining using high-frequency impact hammer in deep hard rock mine. *Trans. Nonferr. Met. Soc. China* **2022**, *32*, 3051–3064. [CrossRef]
18. Zhang, X.Y.; Wang, D.Y.; Peng, Z.L. Effects of high-pressure coolant on cooling mechanism in high-speed ultrasonic vibration cutting interfaces. *Appl. Therm. Eng.* **2023**, *233*, 121125. [CrossRef]
19. Tian, J.L.; Fan, C.Y.; Zhang, T.J.; Zhou, Y. Rock breaking mechanism in percussive drilling with the effect of high-frequency torsional vibration. *Energ. Source. Part A* **2019**, *44*, 2520–2534. [CrossRef]
20. Zhang, L.; Wang, X.F.; Wang, J.Y.; Yang, Z. Mechanical characteristics and pore evolution of red sandstone under ultrasonic high-frequency vibration excitation. *AIP Adv.* **2021**, *11*, 055202. [CrossRef]
21. Yin, S.Y.; Zhao, D.J.; Zhai, G.B. Investigation into the characteristics of rock damage caused by ultrasonic vibration. *Int. J. Rock Mech. Min. Sci.* **2016**, *84*, 159–164. [CrossRef]
22. Pavlovskaia, E.; Hendry, D.C.; Wiercigroch, M. Modelling of high frequency vibro-impact drilling. *Int. J. Mech. Sci.* **2015**, *91*, 110–119. [CrossRef]
23. Li, Z.L.; Wang, L.G.; Li, W.S. Mechanical Behavior and Fracture Characteristics of Rock with Prefabricated Crack under Different Triaxial Stress Conditions. *Minerals* **2022**, *12*, 673. [CrossRef]
24. Yang, Z.B.; Wang, X.F.; Zhang, L.; Wang, J.Y. Research on influencing factors of rock breaking efficiency under ultrasonic vibration excitation. *AIP Adv.* **2023**, *13*, 025160. [CrossRef]
25. Zhao, D.; Han, J.; Zhou, Y.; Lv, X.; Zhang, S.; Gao, K.; Zhao, Y. Rock Crushing Analysis of TBM Disc Cutter Assisted by Ultra-High-Frequency Loading. *Shock Vib.* **2022**, *2022*, 17. [CrossRef]
26. Zhao, Y.; Zhang, C.S.; Zhang, Z.Z.; Gao, K.; Li, J.S.; Xie, X.B. The rock breaking mechanism analysis of axial ultra-high frequency vibration assisted drilling by single PDC cutter. *J. Pet. Sci. Eng.* **2021**, *205*, 108859. [CrossRef]
27. Li, S.Q.; Yan, T.; Li, W.; Bi, F.Q. Modeling of vibration response of rock by harmonic impact. *J. Nat. Gas Sci. Eng.* **2015**, *23*, 90–96. [CrossRef]
28. Huang, J.G.; Wang, H.G.; Ji, G.D.; Zhao, F.; Ming, R.; Hao, Y. The Rock Breaking Mechanism of Ultrasonic High Frequency Rotary-Percussive Drilling Technology. *Pet. Drill. Tech.* **2018**, *46*, 23–29.
29. Li, S.; Yan, L.; Li, W.; Zhao, H.; Ling, X. Research on Energy Response Characteristics of Rock under Harmonic Vibro-Impacting Drilling. *J. Vib. Eng. Technol.* **2019**, *7*, 487–496. [CrossRef]
30. Wang, J.; Yang, M.; Liang, F.; Feng, K.; Zhang, K.; Wang, Q. An Algorithm for Painting Large Objects Based on a Nine-Axis UR5 Robotic Manipulator. *Appl. Sci.* **2022**, *12*, 7219. [CrossRef]

31. Galindo, R.A.; Serrano, A.; Olalla, C. Ultimate bearing capacity of rock masses based on modified Mohr-Coulomb strength criterion. *Int. J. Rock Mech. Min. Sci.* **2017**, *93*, 215–225. [CrossRef]

32. Zhong, Z.; Zhang, H.; Hu, Y.J.; Lou, R.; Tao, P.; Liu, J. Experimental and numerical explorations on the optimized applications of SCDA in cracking concrete blocks. *Measurement* **2023**, *206*, 112335. [CrossRef]

33. Zhang, J.W.; Li, Y.L. Ultrasonic vibrations and coal permeability: Laboratory experimental investigations and numerical simulations. *Int. J. Min. Sci. Technol.* **2017**, *27*, 221–228. [CrossRef]